



University of Tennessee, Knoxville
**Trace: Tennessee Research and Creative
Exchange**

Masters Theses

Graduate School

8-2009

Geometrical Effects on Electromagnetic Enhancement to SERS from Metal Nanoparticle Dimer Arrays

Abigail Laurel Gaddis

University of Tennessee - Knoxville

Recommended Citation

Gaddis, Abigail Laurel, "Geometrical Effects on Electromagnetic Enhancement to SERS from Metal Nanoparticle Dimer Arrays. " Master's Thesis, University of Tennessee, 2009.
https://trace.tennessee.edu/utk_gradthes/78

This Thesis is brought to you for free and open access by the Graduate School at Trace: Tennessee Research and Creative Exchange. It has been accepted for inclusion in Masters Theses by an authorized administrator of Trace: Tennessee Research and Creative Exchange. For more information, please contact trace@utk.edu.

To the Graduate Council:

I am submitting herewith a thesis written by Abigail Laurel Gaddis entitled "Geometrical Effects on Electromagnetic Enhancement to SERS from Metal Nanoparticle Dimer Arrays." I have examined the final electronic copy of this thesis for form and content and recommend that it be accepted in partial fulfillment of the requirements for the degree of Master of Science, with a major in Physics.

Zhenyu Zhang, Major Professor

We have read this thesis and recommend its acceptance:

Lee Riedinger, Hanno Weitering, Robert Compton

Accepted for the Council:

Dixie L. Thompson

Vice Provost and Dean of the Graduate School

(Original signatures are on file with official student records.)

To the Graduate Council:

I am submitting herewith a thesis written by Abigail Laurel Gaddis entitled "Geometrical Effects on Electromagnetic Enhancement to SERS from Metal Nanoparticle Dimer Arrays." I have examined the final electronic copy of this thesis for form and content and recommend that it be accepted in partial fulfillment of the requirements for the degree of Master of Science, with a major in Physics.

Zhenyu Zhang, Major Professor

We have read this thesis
and recommend its acceptance:

Lee Riedinger

Hanno Weitering

Robert Compton

Accepted for the Council:

Carolyn R. Hodges
Vice Provost and Dean of the Graduate School

Geometrical Effects on Electromagnetic Enhancement to Raman Scattering from Metal Nanoparticle Dimer Arrays

A Thesis Presented for
the Master of Science
Degree
The University of Tennessee, Knoxville

Abigail Laurel Gaddis
August 2009

Copyright © 2009 by Abigail Laurel Gaddis
All rights reserved.

Acknowledgements

I am grateful to my colleague Ke Zhao for many helpful conceptual discussions and programming supervision. I am indebted to my advisor Dr. Zhenyu Zhang for his guidance, knowledge, and motivation for completing this work. The cooperation of Dr. Zhang's theoretical condensed matter group at ORNL was important to my progress. I appreciate the help of the experimental group under Dr. Baohua Gu with providing experimental data and software. I would like to thank Dr. Chun-Hway Hsueh for conversations about FDTD modeling and sharing computational results. I wish to thank Dr. Lee Riedinger for providing advice and encouragement, as well as Dr. Robert Compton and Dr. Hanno Weitering for serving on my committee. The knowledgeable staff at Lumerical Solutions technical support has been very helpful in completing my research. I am grateful to my family and friends for their support, understanding, and encouragement during this process.

Abstract

Much recent effort has been devoted to the study of the optical properties of metal nanoparticle substrates. In such finely ordered structures, surface plasmons can be induced by incident light. These collective excitations of the electrons in the nanoparticle create localized areas of high electromagnetic field intensity. The intense local fields generated are of interest for various applications, including Surface-enhanced Raman Scattering (SERS) for molecular detection and sensing. In this thesis, the optical properties of various nanoparticle dimer and array geometries are considered, including gold triangular prism dimers and silver spherical dimers. The effect of SERS due to electromagnetic interaction of the metal nanoparticles with incident light is computed using the finite-difference time-domain (FDTD) method. These results are compared with those from generalized Mie theory simulations and recent experimental work. The positions, wavelengths, and magnitudes of maximum electric field enhancement for different geometries are presented. These findings may serve as important guidance in future design of nanoplasmonic devices.

Table of Contents

Chapter 1	Introduction	1
Chapter 2	Electrodynamics of Metal Nanoparticles	4
2.1	Plasmons	4
2.2	Nanogap Effect	5
2.3	Nanoparticle Arrays	6
2.4	Raman Scattering	6
2.5	Surface-Enhanced Raman Scattering	7
Chapter 3	Computational Algorithms	9
3.1	Mie Theory	9
3.1.1	Coupled dipole approximation	9
3.1.2	T-matrix method	10
3.2	FDTD	10
3.2.1	Yee algorithm	10
3.2.2	Numerical dispersion	13
3.2.3	Nonlinear and dispersive media	13
3.2.4	Source wave conditions	14
3.2.5	Absorbing boundary conditions	15
3.2.6	Periodic structures	15
Chapter 4	Recent Motivating Results	16
4.1	Spherical Dimer	16
4.2	Triangular Prism Dimer	16
4.3	Triangular Prism Dimer Array	18
4.4	Other Geometries	19
Chapter 5	Simulation Models	20
5.1	Spherical Dimer	21
5.2	Triangular Prism Dimer	22
5.3	Triangular Prism Dimer Array	24
Chapter 6	Results	28
6.1	Spherical Dimer	28
6.2	Triangular Prism Dimer	29
6.3	Triangular Prism Dimer Array	35
Chapter 7	Discussion	38
7.1	Comparison with Computational Results	38
7.2	Comparison with Experimental Results	38
Chapter 8	Conclusion and Outlook	40

List of Figures

Figure 3.1: Yee cell, <i>After</i> : [24].	12
Figure 4.1: Scanning electron micrograph of SERS substrate [26].	17
Figure 5.1: Spherical silver dimer setup	21
Figure 5.2: Gold triangular prism dimer setup	23
Figure 5.3: Gold bowtie array, low-density test	25
Figure 5.4: Gold bowtie array, high-density test	25
Figure 5.5: Gold bowtie array, low-density periodic boundaries	26
Figure 5.6: Gold bowtie array, high-density periodic boundaries	27
Figure 6.1: Silver Spherical Dimer at resonance wavelength	28
Figure 6.2: Silver Spherical Dimer at the origin	29
Figure 6.3: Gold Bowtie at resonance wavelength, height 40nm, gap 10nm	30
Figure 6.4: Gold Bowtie at the origin, height 40nm, gap 10nm	30
Figure 6.5: Gold Bowtie at resonance wavelength, height 50nm, gap 10nm	31
Figure 6.6: Gold Bowtie at the origin, height 50nm, gap 10nm	31
Figure 6.7: Gold Bowtie at resonance wavelength, height 30nm, gap 10nm	32
Figure 6.8: Gold Bowtie at the origin, height 30nm, gap 10nm	32
Figure 6.9: Gold Bowtie at resonance wavelength, height 20nm, gap 10nm	33
Figure 6.10: Gold Bowtie at the origin, height 20nm, gap 10nm	33
Figure 6.11: Gold Bowtie at resonance wavelength, height 40nm, gap 20nm	34
Figure 6.12: Gold Bowtie at the origin, height 40nm, gap 20nm	34
Figure 6.13: Gold bowtie array, high-density, initial test	35
Figure 6.14: Gold bowtie array, low-density, initial test	35
Figure 6.15: Gold bowtie array, high-density, at the origin	36
Figure 6.16: Gold bowtie array, high-density, resonance wavelength	37
Figure 6.17: Gold bowtie array, low-density, at the origin	37

Chapter 1

Introduction

As optical technologies push for higher frequency capability and electronics become smaller in size, plasmonics is reaping the benefits of the advances in both fields. Plasmonics is the study of quantized plasma oscillations, also known as plasmons. This field interrogates regions small in size and high in optical frequency. A major area of research in plasmonics is the study of metal nanoparticles. Usually between 1-100 nm in size, these small structures have a wide variety of applications. Some uses include chemical and biological sensing [1,2], optics [1], and optoelectronics [1,3]. Other proposed applications include medical treatments and waveguides [4].

A field that has recently been tied to the study of plasmonics is that of Raman scattering. Raman scattering occurs when a photon is inelastically scattered. Observing the spectrum of a Raman scattered photon yields information about the properties of the scatterer molecule [5]. Light produced by Raman scattering may be enhanced by metal nanoparticles into a more easily detectable signal [6]. Using a construct to enhance the Raman scattering signal is known as surface-enhanced Raman scattering (SERS). It depends strongly on the understanding and fabrication of nanoparticle substrates, so that developments in the field of plasmonics are closely related to advances in the understanding of SERS. Since the inception of the field in the early 1970s, many scientific advances have occurred, allowing for a regrowth of the field in the last decade. A qualitative example of this is the notable increase in publications about SERS in the last decade [7, 8].

Experimental techniques needed to fabricate and characterize nanomaterials as well as measuring the resulting spectra have developed greatly since the first SERS experiment in 1974. Procedures such as electron beam lithography and molecular assembly techniques allow for more precise creation of a wider variety of

nanoscale surfaces. Microscopical methods such as scanning probe microscopes facilitate observation of the surfaces created. Additionally, optical and laser technologies associated with monitoring the induced spectra have also advanced [2].

Further, as electrodynamic computation techniques and resources mature, they provide new ways to understand and model these systems. In 1908, the development of Mie theory led to the possibility of the application of Maxwell's equations to very small spherical objects. Until the 1960s, the majority of solutions to Maxwell's equations were closed-form and analytic, as is the case with Mie theory. As computers became more sophisticated and nanofabrication more capable, solving Maxwell's equations numerically became possible and necessary [1].

Frequency-domain computational techniques were then developed, and matured into methods such as the finite-difference time-domain method (FDTD). These offered the capability of solving Maxwell's differential equations in the time domain using spatial grids for a wide range of problems. These developments allowed more accurate modeling of complex nanoparticle conglomerates that are of interest for SERS.

Furthermore, the wide assortment of applications of SERS has kept interest in the topic high. Chemical and biological sensing [9], especially single molecule detection, is an important motivation for this research. SERS can potentially also be used to characterize thin films, nanoparticle colloids, and nanocomposite films [10].

In this work, the optical properties of various nanoparticle dimer and array geometries are calculated, including those of gold triangular prism dimers and silver spherical dimers. The effect of SERS due to electromagnetic interaction of the metal nanoparticles with incident light is computed using the finite-difference time-domain (FDTD) method. The results obtained are then compared with those from generalized Mie theory simulations and recent experimental work. The positions, wavelengths, and magnitudes of maximum electric field enhancement for these

geometries are discussed. These findings may function as guidance for future design of optical nanoplasmonic devices.

In Chapter Two, the theoretical background behind the electrodynamics of metal nanoparticles is discussed. Chapter Three overviews two commonly used computational algorithms for approximating Maxwell's equations in these constructs. Next, Chapter Four describes recent experimental and theoretical studies that motivated this work. The simulations done in this work are described in Chapter Five, and the results obtained from these models are outlined in Chapter Six. Chapter Seven compares the work motivating this study with the results found in the FDTD simulations done for this thesis. The final section, Chapter 8, concludes the work and offers outlooks for future research.

Chapter 2

Electrodynamics of Metal Nanoparticles

2.1 *Plasmons*

In a metal exposed to an electric field, the conduction electrons move along the electric field lines, while the positive nuclear cores remain in place. This charge displacement results in an electric dipole field. This collective excitation of electrons in the conduction band is known as a plasmon. More succinctly, a plasmon is an oscillation of an electron cloud against the fixed positive ions of the metal.

If a time-dependent incident electric field is introduced, the electrons in the metallic structure oscillate with a certain frequency known as the plasmon frequency. For instance, if the source excitation is light, the incident electric field vector varies in time, inducing the oscillation of the electrons. The plasmon frequency depends on the size of the metal structure, the shape of the structure, and the density of conduction electrons [2]. For example, it has been found that as the size of the metal particle decreases, the frequency of the plasmon increases [2, 11]. In addition, the electron density is directly related to the identity of the chemical element [2]. Therefore the type, shape, and size of material used are important for plasmon frequency determination.

Further, when the incident light frequency is near the plasmon frequency, resonance occurs. For very small particles, quantum effects dominate, and the coherence of the plasmon degenerates [7]. For small particles, the field generated by the scattered light is similar to dipole radiation. As the size of the particle increases, higher multipoles are generated [4, 2]. For particles with size on the order of the incident wavelength, higher-order non-radiative multipoles are excited [7]. Either size-limiting case decreases the intensity of the scattered light. However, at

the resonance wavelength, the electromagnetic fields generated have high local intensities.

In order to create this resonance, an interest has developed in studying the behavior of plasmons in very small structures above the quantum interference limit, known as nanoparticles. For metal nanoparticles, excitations at certain frequencies give rise to a surface plasmon resonance.

Since certain materials have a plasmon frequency close to that of visible light, it follows that these materials are advantageous for the intensification of the electric field of incident visible light. Silver and gold are of special interest due to the strength of their absorption band in the visible spectrum [2]. Other metals known to produce surface plasmons include copper and platinum [7].

The shape of the nanoparticle is also significant in determining its resonance behavior. Various studies have shown that the peak field of nanoparticles varies with the shape of the particle; notably, smoother nanoparticles show a smaller $|\mathbf{E}|^2$ value than ones with sharp tips [2, 11, 12, 13].

2.2 Nanogap Effect

Two interacting metal nanoparticles in a time-varying electric field can be characterized as two interacting electric dipoles. The coupling in this system depends on the polarization, direction, and wavelength of the incident light. For instance, polarization parallel to the axis of a spherical dimer has been found to give the highest enhancement in the inter-dimer region [11, 14, 15].

In the region between the nanoparticles, known as the nanogap, the electric field is locally very intense. As the gap between the nanoparticles is decreased, the size of the electromagnetic enhancement in the gap increases [14, 16, 17]. However, as the inter-dimer distance becomes very small, continuum electrodynamics calculations are less reliable [16]. Due to this, calculations of field intensities for gap sizes smaller than 1nm are often overestimates [16].

2.3 Nanoparticle Arrays

In arrays of nanoparticles, surface plasmons can also be induced by incident light on each nanoparticle. Then the metal nanoparticles in such arrays can exhibit coupled plasmon resonances, which can shift the plasmon wavelength [18].

This interaction led scientists to develop solutions of nanoparticles scattered randomly throughout some medium [19]. The ease of manufacture of such colloidal arrays also led to their widespread use. However, lack of structure in the array creates locational control issues.

Furthermore, such unordered arrays fail to take advantage of a second enhancement: for arrays of dimers and other closely spaced arrays, photonic effects arise, leading to additional photonic resonances [19]. The long-range interactions between the fields produced by the incident light on the nanoparticles create localized areas of high electromagnetic field intensity within the structure [16, 20]. The combination of photonic and plasmonic resonances results in even higher localized field intensities than in single nanoparticles, dimers, or colloidal aggregates [18, 19, 21]. Thus, ordered dimer arrays can provide intense local electromagnetic fields.

2.4 Raman Scattering

Discovered in 1928 by C.V. Raman, Raman scattering occurs when a photon is inelastically scattered. Most photons from light incident on atoms or molecules are elastically scattered with no loss of energy, via Rayleigh scattering. However, some are inelastically scattered, losing (or gaining) energy from an excitation (or dexcitation) of the molecule. These energy levels can be vibrational, electronic, or rotational in nature. Observing the spectrum of a Raman scattered photon yields information about the properties of the scatterer molecule [5].

Stokes scattering involves the loss of energy of an incoming photon to a molecular excitation level, while anti-stokes scattering entails a greater final energy

for the photon due to the de-excitation of the thermally excited molecule. Both are inelastic Raman scattering processes. However, in either case the change in energy of the photon is very small, making the characteristic Raman spectra difficult to detect.

2.5 *Surface-Enhanced Raman Scattering*

Due to the attractiveness of Raman spectra and the amplifying properties of nanoparticles, the study of metallic nanoparticle substrates for enhancing Raman scattering is a strong candidate for current research. In a surface-enhanced Raman scattering (SERS) regime, molecules adsorbed on the nanoparticle surfaces in an array experience more intense electronic transitions, and thus, emit more intense Raman spectra. This allows the spectra to be more easily detected [6].

The source of this intensity has been attributed to some combination of chemical and electromagnetic enhancement [16, 20, 21]. The decoupled electromagnetic contribution to SERS enhancement, symbolized here as M^{EM} , can be expressed as $M^{EM} = |\mathbf{E}(\omega)|^2 |\mathbf{E}(\omega')|^2$ where $\mathbf{E}(\omega)$ is the incident local electric field, and $\mathbf{E}(\omega')$ is the Stokes-shifted field [16, 21]. Since the difference between the Stokes-shifted frequency and the original frequency is often within the range of peak of the plasmon [2], a common approximation is that $M^{EM} \cong |\mathbf{E}(\omega)|^4$ [1, 2, 12, 20].

In early efforts, enhancement factors ranging from $10^5 - 10^6$ were reached [20], often with single nanoparticles or spherical dimers [22]. However, this was only strong enough to use SERS as an ensemble average technique. Enhancement factors greater than 10^{13} are required for signal observation of single molecule Raman spectra [16]. Using certain specially manufactured substrates, SERS enhancement factors of 10^{10} and higher have been recorded [11, 20]. It has been recently shown that one can observe signals from single molecules (SMSERS), including the first observation of a single glucose molecule [23].

Finding the maximal substrate for surface-enhanced Raman scattering studies is an ongoing field of research. This involves taking advantage of the characteristics of the nanoparticles themselves as well as their orientation to each other to greatly increase the intensity of Raman spectra.

Chapter 3

Computational Algorithms

Selection of a particular computational technique to solve a specific problem can be difficult. In this work, the finite-difference time-domain method (FDTD) was chosen for several reasons. First, sources of error are well understood because of the long-term development of this method since the 1970s, and these sources of error can be accounted for using known techniques [24]. The solutions generated from this model are in the time domain; as a result, impulse response and nonlinear behavior of systems are treated naturally [24]. Further, the propagation of one electromagnetic impulse provides data for a broad range of frequencies [1]. Another advantage of FDTD is that a wide variety of structures may be modeled [1]. Additionally, the time step nature of the algorithm lends itself to easy visual modeling of the fields with time [24]. Advantages such as these make FDTD a good choice for modeling plasmonic phenomena.

3.1 Mie Theory

Another well-known computational approach is Mie theory. Mie theory is a way of solving Maxwell's equations analytically in closed form for spherical geometries. Developed in 1908 by German physicist Gustav Mie, it was the first theory to have the capability to probe electrodynamic effects on the nanoscale. Thus, many early calculations were done with this theory, and it continued to dominate the field until recently [2].

3.1.1 *Coupled dipole approximation*

Also known as the discrete dipole approximation, this system for solving Maxwell's equations is a refinement of Mie theory. It employs a grid of point dipoles to simulate the field of a certain structure, essentially representing the structure as a

large number of cubes with a certain polarizability associated with the material's dielectric constant [16]. Matrices representing the electric field, the polarization, and the dipole interaction are generated. These are manipulated to form a system of coupled dipole equations, which are then solved iteratively. The induced polarizations are then used to calculate the nanoparticle extinction cross-section. Since this technique is in the frequency domain, the process must be repeated for all frequencies of interest [4].

3.1.2 T-matrix method

This method for solving Maxwell's equations is based on Mie theory. Similarly to the coupled dipole approximation, this method involves the multiplication and inversion of matrices characterizing the fields from the structures as superpositions of dipole fields [20]. Multipolar expansions around each nanoparticle or other electromagnetically interacting structure are combined, and boundary conditions are applied. From this process, electromagnetic fields are determined, even for large arrays [21].

3.2 **FDTD**

This solution method solves Maxwell's coupled curl equations for both the electric and magnetic fields in space and time. FDTD propagates an incident field in a computational space by updating the electric and magnetic field components at discrete half-step intervals in space and time. This staggered grid method leads to second-order central difference approximations. When the introduced wave no longer interacts with the structure, $\mathbf{E}(r,t)$ is Fourier transformed to give the frequency-dependent field.

3.2.1 Yee algorithm

Maxwell's curl equations for isotropic, linear, nondispersive materials are as follows, in MKS units,

$$\begin{aligned}\frac{\partial \mathbf{H}}{\partial t} &= -\frac{1}{\mu} \nabla \times \mathbf{E} - \frac{1}{\mu} \mathbf{M} \\ \frac{\partial \mathbf{E}}{\partial t} &= \frac{1}{\varepsilon} \nabla \times \mathbf{H} - \frac{1}{\varepsilon} \mathbf{J}\end{aligned}$$

The vectors \mathbf{D} , \mathbf{H} , and \mathbf{E} have three components which depend on the three spatial Cartesian coordinates; \mathbf{D} is the electric flux density, \mathbf{H} is the magnetic field, and \mathbf{E} is the electric field. Further, \mathbf{M} is the equivalent magnetic current density, \mathbf{J} is the electric current density, ε is the electrical permittivity, and μ is the magnetic permeability. It should be noted that $\mathbf{D} = \varepsilon \mathbf{E} = \varepsilon_r \varepsilon_0 \mathbf{E}$ and $\mathbf{B} = \mu \mathbf{H} = \mu_r \mu_0 \mathbf{H}$, where ε_r and ε_0 are the relative and free space permittivity, also μ_r and μ_0 are the relative and free space permeability, respectively [25].

Noting that materials with these properties attenuate electromagnetic fields through conversion to heat energy, as well as that electric and magnetic current densities may act as independent sources of electromagnetic field energy, one may write $\mathbf{M} = \mathbf{M}_{source} + \sigma^m \mathbf{H}$ and $\mathbf{J} = \mathbf{J}_{source} + \sigma \mathbf{E}$. In this case, σ is the electric conductivity, and σ^m is the equivalent magnetic loss [24].

Writing out each vector component of the curl operators in Cartesian coordinates yields the following six coupled equations:

$$\begin{aligned}\frac{\partial H_x}{\partial t} &= \frac{1}{\mu} \left[\frac{\partial E_y}{\partial z} - \frac{\partial E_z}{\partial y} - (M_{source_x} + \sigma^m H_x) \right] \\ \frac{\partial H_y}{\partial t} &= \frac{1}{\mu} \left[\frac{\partial E_z}{\partial x} - \frac{\partial E_x}{\partial z} - (M_{source_y} + \sigma^m H_y) \right] \\ \frac{\partial H_z}{\partial t} &= \frac{1}{\mu} \left[\frac{\partial E_x}{\partial y} - \frac{\partial E_y}{\partial x} - (M_{source_z} + \sigma^m H_z) \right] \\ \frac{\partial E_x}{\partial t} &= \frac{1}{\varepsilon} \left[\frac{\partial H_z}{\partial y} - \frac{\partial H_y}{\partial z} - (J_{source_x} + \sigma E_x) \right] \\ \frac{\partial E_y}{\partial t} &= \frac{1}{\varepsilon} \left[\frac{\partial H_x}{\partial z} - \frac{\partial H_z}{\partial x} - (J_{source_y} + \sigma E_y) \right] \\ \frac{\partial E_z}{\partial t} &= \frac{1}{\varepsilon} \left[\frac{\partial H_y}{\partial x} - \frac{\partial H_x}{\partial y} - (J_{source_z} + \sigma E_z) \right]\end{aligned}$$

From these equations, Yee developed a set of centered finite-difference expressions in three dimensions. These expressions cyclically calculate electromagnetic field vector components based on their previous value, the previous values of the other field vector at adjacent points, and the known electric and magnetic current sources [1, 24].

For example, to take the central difference for the E_x component at $E_x|_{i,j+1/2,k+1/2}^n$, in the style of [24], one would take the central difference of both sides of the curl equation for the E_x component. Then one would apply a semi-implicit approximation: that the E_x values at time step n are the average of the previous time step E_x value and the next E_x value. Algebraic manipulation then yields the equation for the time stepping of the E_x

component:

$$E_x|_{i,j+1/2,k+1/2}^{n+1/2} = \left(\frac{1 - \frac{\sigma_{i,j+1/2,k+1/2}\Delta t}{2\epsilon_{i,j+1/2,k+1/2}}}{1 + \frac{\sigma_{i,j+1/2,k+1/2}\Delta t}{2\epsilon_{i,j+1/2,k+1/2}}} \right) E_x|_{i,j+1/2,k+1/2}^{n-1/2} + \left(\frac{\frac{\Delta t}{\epsilon_{i,j+1/2,k+1/2}}}{1 + \frac{\sigma_{i,j+1/2,k+1/2}\Delta t}{2\epsilon_{i,j+1/2,k+1/2}}} \right) \cdot \left(\frac{H_z|_{i,j+1,k+1/2}^n - H_z|_{i,j,k+1/2}^n}{\Delta y} - \frac{H_y|_{i,j+1/2,k+1}^n - H_y|_{i,j+1/2,k}^n}{\Delta z} - J_{source_x}|_{i,j+1/2,k+1/2}^n \right)$$

Similarly, one may readily derive the expressions for the time progression of the other five components [24].

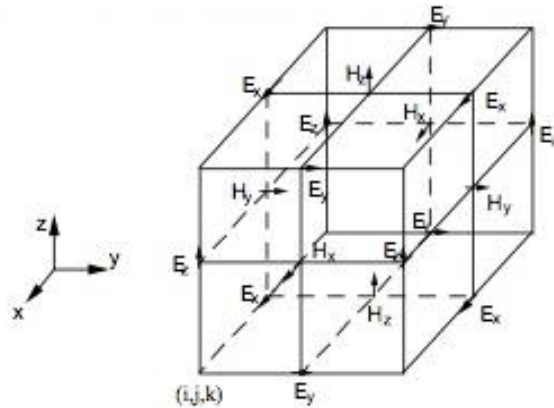


Figure 3.1: Yee cell, similar to Taflove [24].

One way to visualize the interleaving of the components is through the examination of a Yee cell (Figure 3.1). Due to this updating scheme of the algorithm, the computation is easily parallelized [24]. It should be noted that while there are several programming techniques to minimize the data stored for each grid point, another consequence of the updating system of the algorithm is the memory required for the simulation is directly related to the size of the grid employed [24].

3.2.2 Numerical dispersion

While the time-stepping algorithm is non-dissipative, the FDTD algorithms do cause nonphysical dispersion of the simulated waves in the computational lattice [24]. The numerical wave dispersion equation for the Yee algorithm has been derived previously [24] to

$$\text{be: } \left[\frac{1}{c\Delta t} \sin\left(\frac{\omega\Delta t}{2}\right) \right]^2 = \left[\frac{1}{\Delta x} \sin\left(\frac{\tilde{k}_x \Delta x}{2}\right) \right]^2 + \left[\frac{1}{\Delta y} \sin\left(\frac{\tilde{k}_y \Delta y}{2}\right) \right]^2 + \left[\frac{1}{\Delta z} \sin\left(\frac{\tilde{k}_z \Delta z}{2}\right) \right]^2$$

In the limit as Δx , Δy , Δz , and Δt approach zero, it can be seen that this equation reduces to the dispersion relation for a plane wave in a lossless medium:

$\left(\frac{\omega}{c}\right)^2 = (k_x)^2 + (k_y)^2 + (k_z)^2$. Thus, as the grid spacing and time step spacing are reduced, numerical dispersion is minimized.

3.2.3 Nonlinear and dispersive media

Computational models must take into account materials with frequency-dispersive, nonlinear, and gain dielectric properties. Three important classes of linear, isotropic material dispersions are Debye, Lorentz, and Drude media. Debye and Lorentz media are both characterized by complex-valued frequency functions, while the Drude model is employed to account for interior electron motion in metals. FDTD calculations manage such materials by enforcing the appropriate boundary condition on the field components at the interfaces of media [24].

3.2.4 *Source wave conditions*

One modeling issue in FDTD programming is the question of how to introduce the physics of a light source accurately, yet in a manner compact enough spatially to minimize the computer storage and running time of the simulation. There are several classes of such electromagnetic wave sources, including hard-sourced fields, electric and magnetic current sources, the total field/scattered field formulation, and waveguide sources [24].

Hard-sourced fields and current sources create problems when simulating plane waves [24]. Thus, the method preferred for realizing pulses for long durations is the total field/scattered field formulation. This method presumes that the total electric and magnetic fields may be characterized as a summation of their incident and scattered components. Since the Yee algorithm can operate equally well on the total field, the scattered field, or the incident field, it is possible to divide the Yee grid into two regions [24].

In one region, the central region surrounding the interacting structure, the total field is calculated and propagated in the Yee algorithm. In the second region, from the edge of the first region to the end of the simulation, only the scattered field is propagated. This division allows for an arbitrary incident wave, and simplicity in the introduction of the wave. The incident field need only be calculated along the rectangular virtual surface between the two regions [24].

When the Yee algorithm takes the central difference along the virtual boundary between the two regions, a discrepancy appears. On the total field side of the boundary, the field reported is the total field, however, in the second region the field is assumed to be only the scattered field. Thus, along this boundary an adjustment must be made to correct the ongoing algorithm computations. The addition of a known incident field term resolves this problem [1, 24].

3.2.5 Absorbing boundary conditions

In the FDTD method, absorbing boundary conditions are needed to model radiation effects. Ideally, absorbing boundary conditions reflect none of the radiation, absorbing all the outgoing radiation. This simulates the waves extending to infinity while still having a defined computational region.

Since the simulation region is truncated at the boundary, central differences cannot be taken there. The required half-cell spacing would be outside the lattice. Each absorbing boundary condition implementation method must take this into account.

One commonly used absorbing boundary condition is known as a perfectly matched layer [1]. Berenger introduced this method in 1994 to eliminate some of the difficulties with previous absorbing boundary conditions [24]. By splitting each vector field component in Maxwell's equations into two orthogonal components, he developed a set of 12 coupled, partial-differential equations. Next, the choice of appropriate loss parameters allows a planar interface consistent with a dispersionless medium to be derived [24]. As more layers are added, the non-physical reflections from the boundary conditions decrease exponentially [24].

3.2.6 Periodic structures

When modeling arrays in FDTD software, one is often replicating a central structure over and over. As the structure is replicated and the size of the model increases, the computation time and memory demands can soon become unmanageable. Rather than modeling the entire array, one may enforce periodic boundary conditions on a model of the base structure [1][26]. This mimics the effect of an array without the high computational demand [24].

Chapter 4

Recent Motivating Results

Recent computations and experiments, including unpublished work of colleagues at Oak Ridge National Laboratory, motivate the selection of structures and geometries studied in this work. The objective of these studies is to find the optimal nanoparticle arrangement for SERS enhancement.

4.1 *Spherical Dimer*

Mie theory-based computations for a solid silver spherical dimer have been done [12]. For this calculation, the radius of each sphere was 45nm, and the inter-dimer spacing was 5.5nm. This work found the highest enhancement to occur when the incident electric field vector was parallel to the dimer axis. Further, it also found that the highest enhancement was given when the polarization vector was also parallel to the dimer axis. For the setup with the polarization vector parallel the dimer axis, the resulting M^{EM} value was highest in the center of the dimer at about $\lambda = 400$ nm and had a magnitude of approximately 6×10^6 [12].

4.2 *Triangular Prism Dimer*

Experimental colleagues at Oak Ridge National Laboratory have done recent work with gold nanoparticles [26]. As part of a large body of fabricated structures, single triangular prism dimers, also known as “bowties,” were created with a base length and height of 100nm (Figure 4.1). Thionine and p-Aminothiophenol (p-ATP) molecules were adsorbed on the surface of the bowties, with an approximate thickness of 0.5 nm. These bowties were supported by a substrate of Si with an 8 nm thick Cr coating.

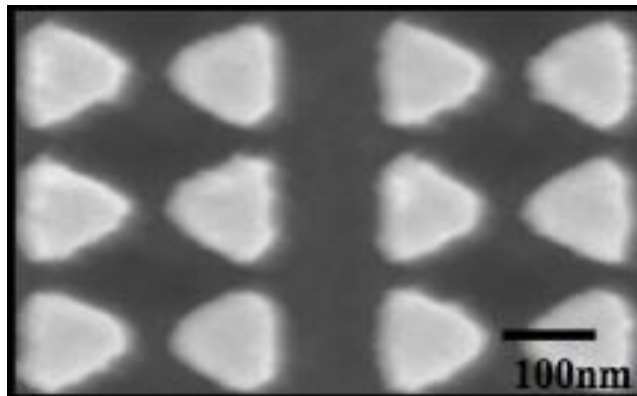


Figure 4.1: Scanning electron micrograph of a SERS substrate fabricated by the experimental group, consisting of gold triangular prism nanoparticle dimers in an array [26].

These structures were illuminated by light with different polarization directions. For the bowties, the optimal polarization direction was found to be polarization across the dimer axis (called “parallel”).

Three different thicknesses were measured: 20, 40, and 60nm prism heights were compared. While the Raman spectra for the adsorbed thionine molecules on the structure remained unchanged in shape, the amplitude of the peak intensity was largest for the 40nm thickness.

Next, the effect of nanotriangle size was explored by comparing the 100x100nm triangles to 200x200nm and 300x300nm cases. Again the SERS spectra were unchanged in shape, but the highest peak values occurred for the 100x100nm triangles.

Then the effect of gap size was investigated using 10, 20, 30, 40, and 50nm gaps. It was found that that the 10nm gap gives the highest Raman intensity, and as the size of the gap increases, the Raman intensity decreases. This was true for both Raman scatterers tested: thionine and p-ATP. This is consistent with previously mentioned studies.

4.3 *Triangular Prism Dimer Array*

Further, these Raman intensities were compared in two densities of arrays. One array, labeled “low density”, contains 20 bowties with a dimer-dimer spacing of $2\mu\text{m}$, and a gap size of 10-50nm. A second array contains 120 bowties with a dimer-dimer spacing of 100nm, and a gap size of 10-50nm.

It was found that the SERS enhancement factor was higher for the high-density array than for the low-density array. For the high-density p-ATP array, the overall enhancement factor was found to be 1.4×10^9 , while for the low density p-ATP array, the overall enhancement factor was measured as 1.0×10^8 .

For the triangular prism dimer array, the polarization of the incident light was shown to have a strong effect on the resulting intensity. As has been previously found, this result states that for maximum SERS enhancement, incident light is polarized along the axis of the dimer.

Further, an associated computational group led by Chun-Hway Hsueh has simulated a dimer array structure based on these experimental characteristics [27]. Bowties with a triangle side length of 100 nm were modeled, similar to the experimental setup. The gap between the two triangles in the bowtie was 50 nm. The thickness of each triangle was 40 nm with a 0.5 nm p-ATP layer on the top surface of the bowtie. The experimental substrate of Si with an 8 nm thick Cr coating was also included in his simulation. The incident light is a plane wave with a span of 500 to 1000 nm in wavelength, and is polarized across the gap between triangles (i.e., along the x-direction). The incident wave is propagating in the negative z-direction. The dimensions of the simulation domain are 420 nm x 300 nm x 1000 nm. Periodic boundary conditions are used in the x-y directions and perfectly matched layers are used at the top and the bottom of the simulated domain to completely absorb waves leaving the simulation domain in the wave propagation direction.

Preliminary results from this study indicate that E_x intensity reaches a maximum at around $\lambda = 680$ nm. However, as the wavelength increases, the x-position of the maximum enhancement likewise increases. Thus, at $\lambda > 580$ nm, the maximum enhancement location moves outside the dimer gap region. Therefore, $|E_x|^2$, the intensity of the dominant electric field component, was calculated at a value less than the peak value, and was found to be approximately 1.8×10^3 . For this incident light setup, the E_x component is larger than the other two field components by orders of magnitude. Thus, it is possible to approximate that $M^{EM} \cong |\mathbf{E}|^4 \cong |E_x|^4$. This would yield a value for M^{EM} of approximately 3.2×10^6 .

4.4 Other Geometries

Other geometries fabricated and illuminated include gold arrays of ellipses, disks, squares, and hexagons, all with inter-dimer gaps of approximately 50nm. The signal response of the triangular prism dimer array in the nanogap was the strongest of any of these geometries. Therefore, the main focus of the experimental and subsequent computational work has been on the bowtie dimer and dimer arrays.

Chapter 5

Simulation Models

FDTD Solutions software was used to facilitate the analysis of nanoparticle structures to provide comparison with previous research. This software provides a CAD -like layout environment with structural and orientational flexibility for nanoshapes in three dimensions. One interesting capability of the program is its ability to generate structures from imported scanning electron microscope image files [28].

Additionally, the simulation grid can be automatically generated uniformly or non-uniformly, and override regions of higher mesh accuracy can be set.

Rather than using Debye, Lorentz, or Drude media models, the software uses a proprietary and highly accurate multi-coefficient method to represent the dielectric functions of the materials [29]. This method is capable of fitting imported experimental dielectric function data or values from other compilations.

Many radiation sources may be modeled, including the preferred total field/scattered field formulation. This source type was used throughout the simulations done for this work.

Various monitor types are available to measure the response of the physical structure to the incident radiation in the simulation. Monitor types include: refractive index monitors, time- and frequency-domain monitors, and movie monitors. Time-domain monitors record information for field components at set intervals in time for a region in space. Frequency-domain profile monitors collect field profile data in the frequency domain for some spatial volume or area. Frequency-domain power monitors aggregate high-accuracy information about the power flow in the frequency domain for a spatial region. Finally, index monitors record n and k values as a function of frequency or wavelength in the simulation.

When the setup is finished the FDTD Solutions software runs the simulation using the FDTD algorithm with the desired settings. The frequency profile monitor of FDTD Solutions software returns the intensity of each component, for instance, $|E_x|^2$. For each simulation, the total electric field intensity was calculated from the components, and this was plotted. From the values for the electric field intensity, the peak electromagnetic enhancement is inferred.

5.1 Spherical Dimer

To test the capability of the FDTD software as well as to confirm previous results, FDTD calculations were performed for a spherical silver dimer (Figure 5.1). Two identical silver spheres with radii of 45nm and a nanogap of 5.5nm were modeled so that the center of their nanogap was the origin. The Johnson and Christy dielectric reference data for silver was used for both spheres [30]. The polarization was parallel to the dimer axis, and the electric field vector was perpendicular to this setup. This correlates to the settings for the spherical dimers modeled by Xu [12].

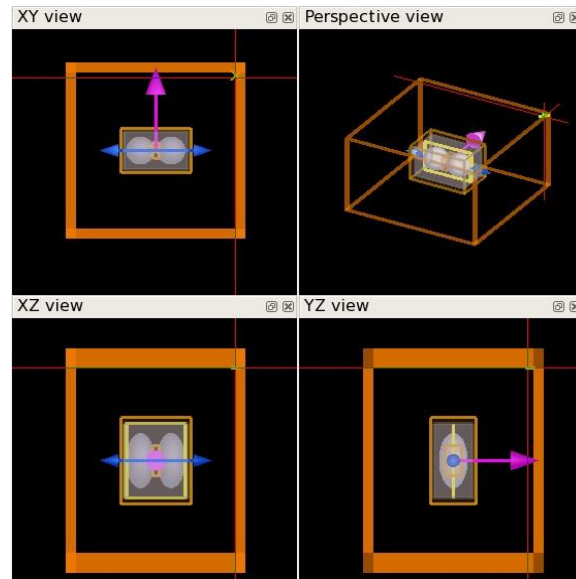


Figure 5.1: Software setup for the spherical silver dimer. The purple arrow indicates electric field propagation direction; the blue arrow indicates polarization direction.

A centered simulation grid with nonuniform spacing was bounded in all directions with two perfectly matched layers. The x -and y- span were both 500 nm, while the z-span was 300nm. Overriding meshes were set to ensure finer grid spacing at points of interest. A grid with spacing set to 5nm was created around the spheres, from -70 to +70nm in the z and y directions, -110 to 110 nm in the x direction. Since it is known that the nanogap region often shows a rapid increase in electric field intensity, a 1nm step size was set in the nanogap to allow finer gradation in the results. This second submesh was also centered at the origin; the x-span was 20nm, while the y- and z-spans were 50nm.

A total field - scattered field source was used. Light was injected from the z-axis in the forward direction and polarized across the dimer axis along the x-direction. The incident light had a wavelength range from 300-800nm, with the center at 550nm. The total field area spanned 200nm in the x-direction and 120nm in the y- and z- directions.

Four monitors were used: two time monitors, a movie monitor, and a frequency domain profile monitor. The movie monitor recorded the electric field intensity in the x-z plane throughout the simulation. The frequency monitor was two dimensional and y-normal as well, recording information about the intensity of each component of the electric field. The time monitors recorded the field at specific time intervals to check for continuity.

5.2 *Triangular Prism Dimer*

Motivated by the experimental findings that this “bowtie” structure shows the strongest response out of several geometries in large arrays, this structure was modeled. While the experimental setup involved large arrays, this computation seeks to support the trends noted in the arrays by simulating a single dimer with variations in nanoparticle thickness and nanogap size. To support the experimental trends noted with gap spacing and thickness of the dimer, a more widely spaced dimer and dimers of various thicknesses were replicated with the FDTD software

(Figure 5.2). Since the material used in the experiment was gold, gold nanoparticles were simulated with dielectric constants calculated again from Johnson and Christy reference data [30]. In the experiment, the p-ATP layer and the Si-Cr substrate are common to all of the bowtie dimer arrays. Since the purpose of the simulation was structural comparison, these experimental specifics are not modeled.

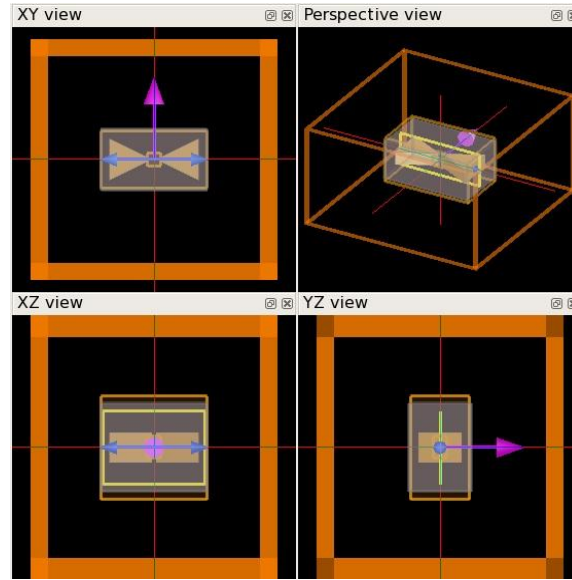


Figure 5.2: Software setup for the gold triangular prism dimers. The purple arrow indicates electric field propagation direction; the blue arrow indicates polarization direction.

First, bowtie dimers with a gap spacing of 10nm and 20nm were simulated in order to compare the effects of inter-dimer spacing on the field and to uphold experimental results. Next, thickness comparisons were performed to support the experimental results. With the 10nm gap setting, thicknesses of 20nm, 30nm and 50nm were compared to the initial 40nm thick dimer.

The simulation settings for all of the gold triangle dimers were the same. A centered simulation grid with nonuniform spacing was again bounded in all directions with two perfectly matched layers. The x- and y- span were both 500 nm, while the z-span was 300nm. An overriding mesh was set in the nanogap region with a 1nm step size. Centered at the origin, its x-, y-, and z-span were 30nm.

As for the spherical dimer, a total field - scattered field source was used. Light was injected from the y-axis in the forward direction and polarized across the dimer axis along the x-direction. The incident light had a wavelength range from 300-800nm, with the center at 550nm. The total field area spanned 300nm in the x- and y- directions and 120nm in the z-direction.

A movie monitor recorded the electric field intensity in the x-y plane throughout the simulation. Also, a two-dimensional frequency monitor recorded information about the intensity of each component of the electric field in the x-y plane.

5.3 Triangular Prism Dimer Array

To compare with the bowtie array experimental setup, similar arrays were modeled. In both arrays, the inter-dimer spacing was 10nm, and the height of the triangular prisms in the z-direction was 40nm. The arrays were one layer thick, in other words, a two-dimensional array in the x-y plane. As in the dimer case, the p-ATP layer and the Si-Cr substrate are not modeled.

As an initial test, two arrays were modeled containing 20 bowties (40 gold triangular nanoparticles), arranged in 4 columns (y-direction) and 5 rows (x-direction). The low-density array had a spacing between dimers in both the x- and y-directions equivalent to $2\mu\text{m}$ or 2,000nm (Figure 5.3). Additionally, a denser bowtie array was processed. Rather than including more nanotriangle pairs as well as a closer spacing as was done in the experiment, the same number of dimers as in the first lower density array was used in order to explore the role of dimer-dimer spacing in field enhancement. The spacing between dimers in both the x- and y-directions was 100nm (Figure 5.4).

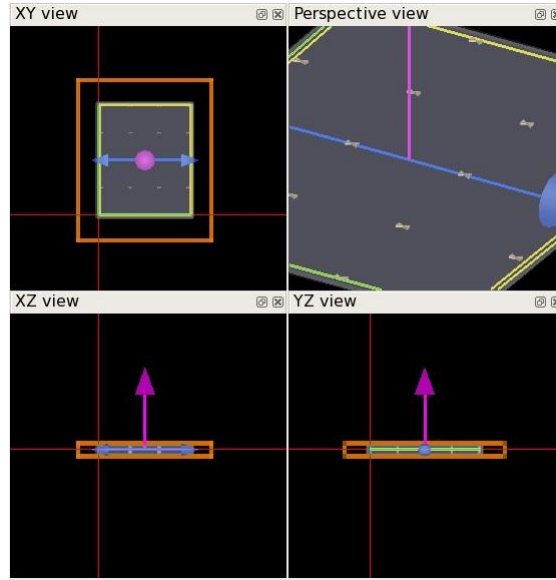


Figure 5.3: Software configuration for the test of the low-density gold bowtie array. The purple arrow indicates electric field propagation direction; the blue arrow indicates polarization direction.

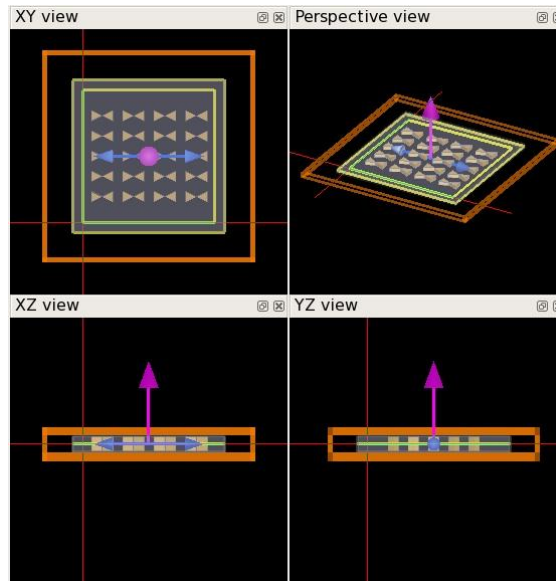


Figure 5.4: Software configuration for the test of the high-density gold bowtie array. The purple arrow indicates electric field propagation direction; the blue arrow indicates polarization direction.

Lastly, the two densities of arrays were again modeled using periodic boundary conditions. A central dimer pair was used as the basis for an array in the x- and y-directions. Settings for both arrays were the same as that of the 40nm high, 10nm gap bowtie arrangement, with the exception of the simulation region. The

dimer-dimer spacings were the same as those of the previously mentioned “low-density” and “high-density” arrays.

For the simulation region of the low-density array, the x-span of the nonuniform grid was 2210nm, while the y-span was 2100nm, and the z-span was 100nm. In the x- and y- directions, periodic boundary conditions were implemented. In the z-direction, the simulation was bounded with two perfectly matched layers (Figure 5.5).

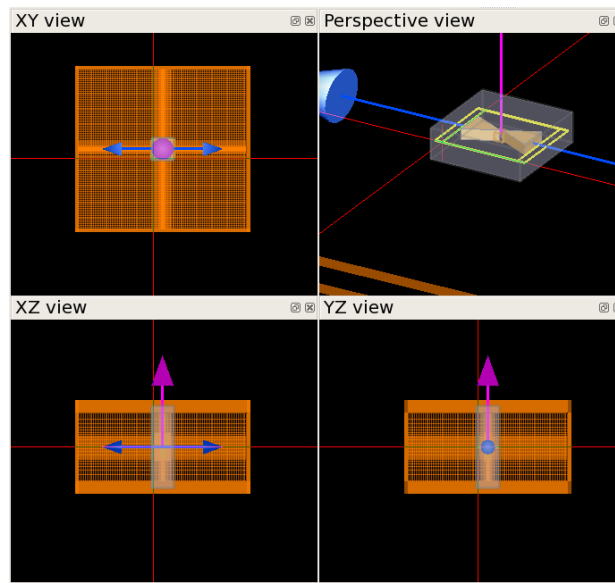


Figure 5.5: Software configuration for the test of the low-density gold bowtie array using periodic boundary conditions. The purple arrow indicates electric field propagation direction; the blue arrow indicates polarization direction.

For the centered nonuniform simulation grid of the high-density array, the x-span was 310nm, the y-span was 200nm, and the z-span was 100nm. Again, in the x- and y- directions, periodic boundary conditions were implemented. However, in the z-direction, the simulation was bounded with two perfectly matched layers (Figure 5.6).

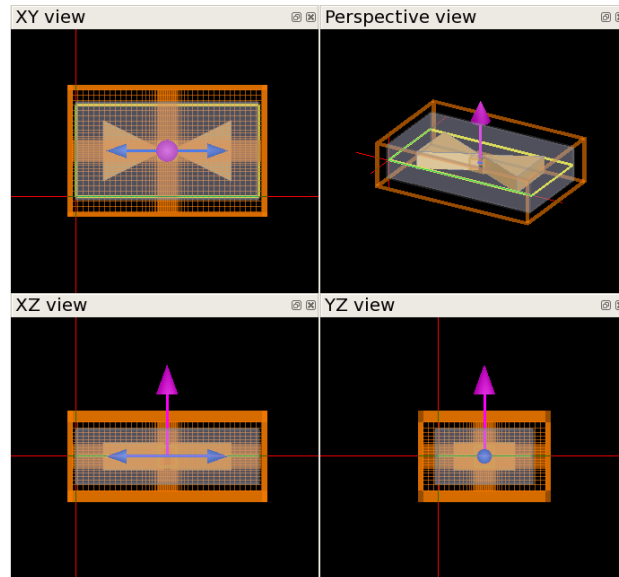


Figure 5.6: Software configuration for the test of the high-density gold bowtie array with periodic boundary conditions. The purple arrow indicates electric field propagation direction; the blue arrow indicates polarization direction.

Chapter 6

Results

6.1 Spherical Dimer

For the silver spherical dimer modeled, qualitative analysis of the E_x intensity versus position graphs at various wavelengths led to the conclusion that the nanogap was indeed the location of highest field enhancement (Figure 6.1). Therefore, the resonance wavelength was evaluated at the origin, and was found to be 440.4nm. The local total electric field intensity at this wavelength, also at the origin, was 4.3×10^3 (Figure 6.2).

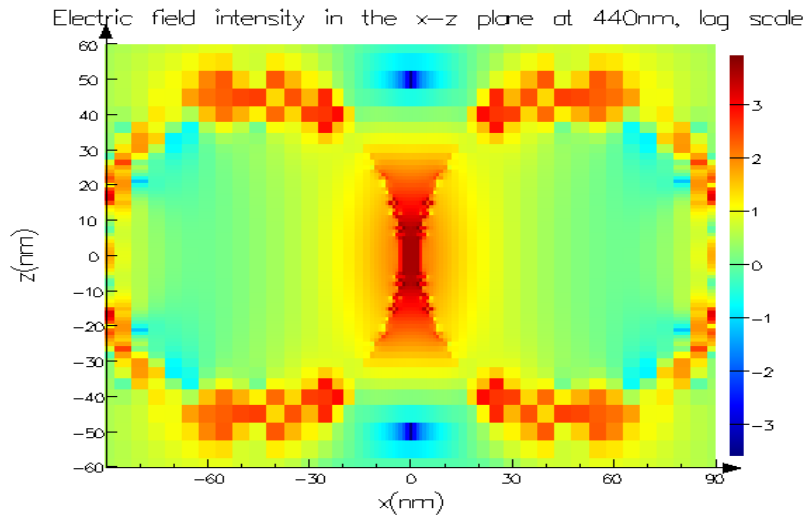


Figure 6.1: Electric field intensity of silver spherical dimer at resonance wavelength of 440nm. Data taken in the x-z plane at $y = 0$ nm.

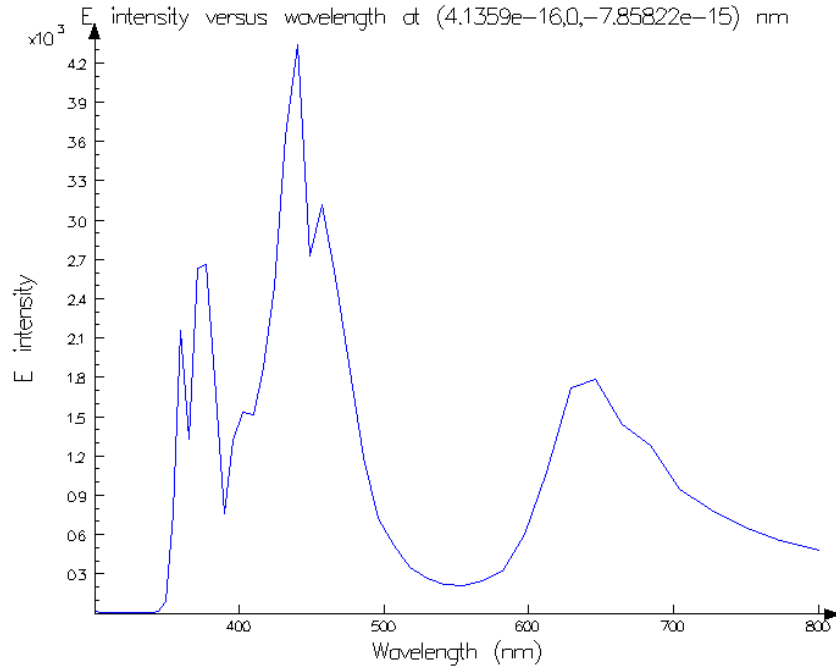


Figure 6.2: Electric field intensity of silver spherical dimer over wavelengths from 300 – 800nm at the origin.

6.2 Triangular Prism Dimer

For the gold triangular prism dimer with a thickness of 40nm and a gap of 10nm, qualitative study of the intensity versus x-y position graph (Figure 6.3) inferred that the nanogap was again the location of highest field enhancement. Evaluated at the origin, the resonance wavelength was found to be 773.7nm. The local field intensity at this wavelength was 3.9×10^3 (Figure 6.4).

For the 50nm thick bowtie with a 10nm gap, the nanogap again contained the regions of highest electric field enhancement (Figure 6.5). Evaluated at the origin, then, the resonance wavelength was found to be 773.7nm, which is about the same as the 40nm dimer. The local field intensity at this wavelength was 2.9×10^3 (Figure 6.6), less than the 40nm dimer.

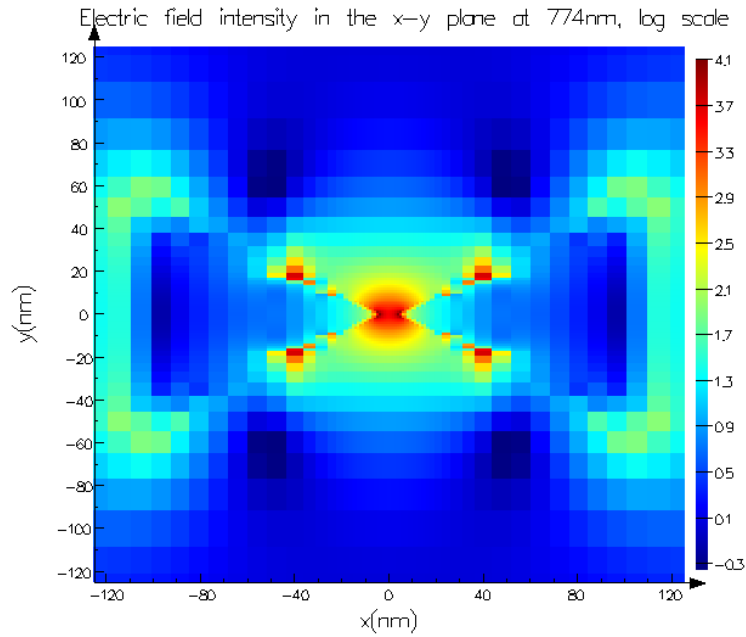


Figure 6.3: Electric field intensity of gold bowtie at resonance wavelength of 774 nm. Data taken in the x-y plane at $z = 0$ nm. Thickness of structure in z direction is 40 nm, nanogap size is 10 nm.

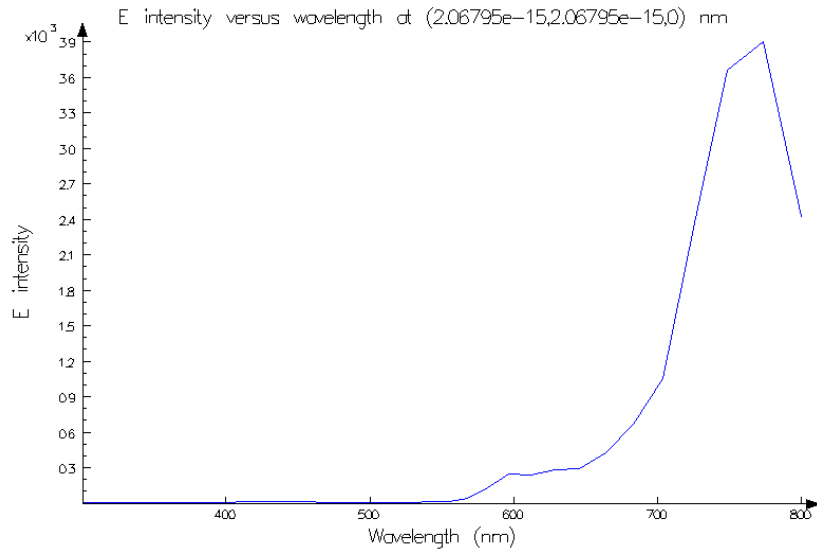


Figure 6.4: Electric field intensity of gold bowtie over wavelengths from 300 – 800 nm at the origin. Thickness of structure in z direction is 40 nm, nanogap size is 10 nm.

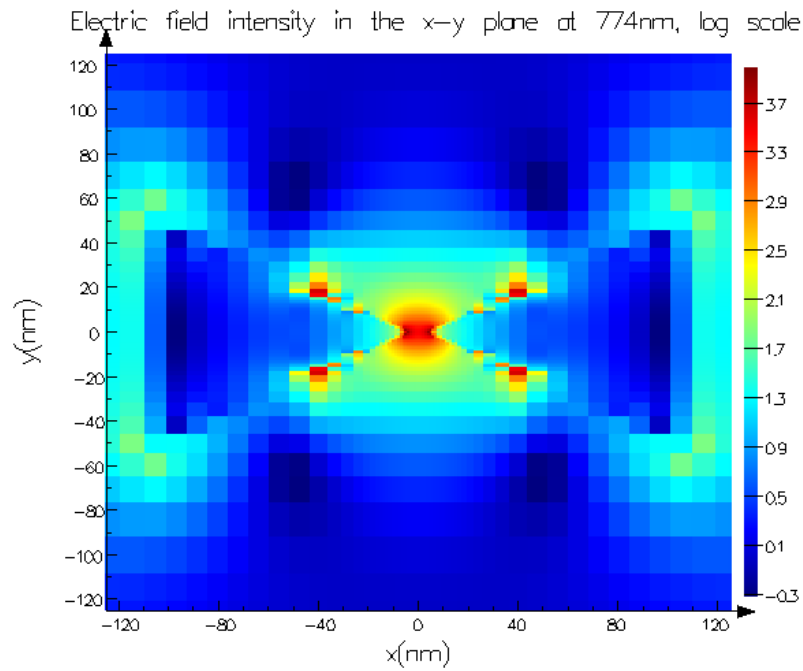


Figure 6.5: Electric field intensity of gold bowtie at resonance wavelength of 774 nm. Data taken in the x-y plane at $z = 0$ nm. Thickness of structure in z direction is 50 nm, nanogap size is 10 nm.

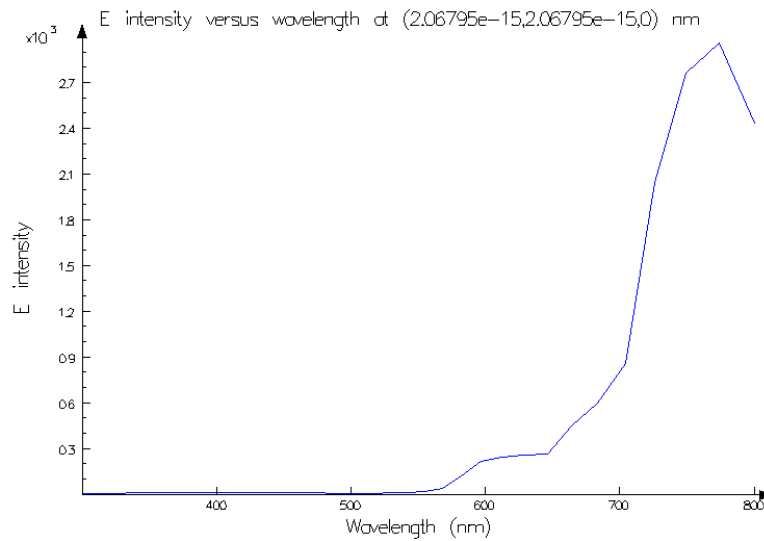


Figure 6.6: Electric field intensity of gold bowtie over wavelengths from 300 – 800 nm at the origin. Thickness of structure in z direction is 50 nm, nanogap size is 10 nm.

For the 30 nm thick bowtie with a 10 nm gap, the most intense electric field was in the inter-dimer region (Figure 6.7). Evaluated at the origin, the resonance

wavelength was found to be 749.0nm, again about the same as the 40nm dimer. The local field intensity at this wavelength was 7.6×10^3 (Figure 6.8).

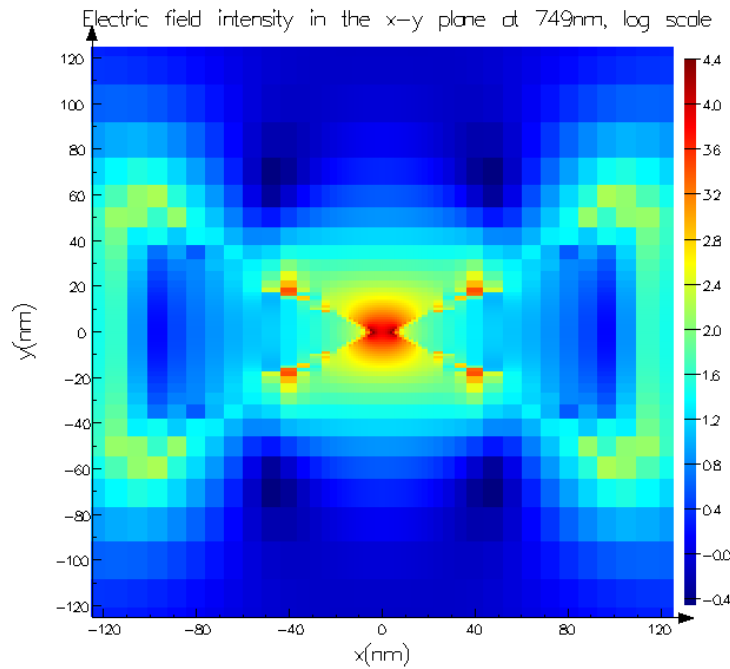


Figure 6.7: Electric field intensity of gold bowtie at resonance wavelength of 749 nm. Data taken in the x-y plane at $z = 0$ nm. Thickness of structure in z direction is 30 nm, nanogap size is 10 nm.

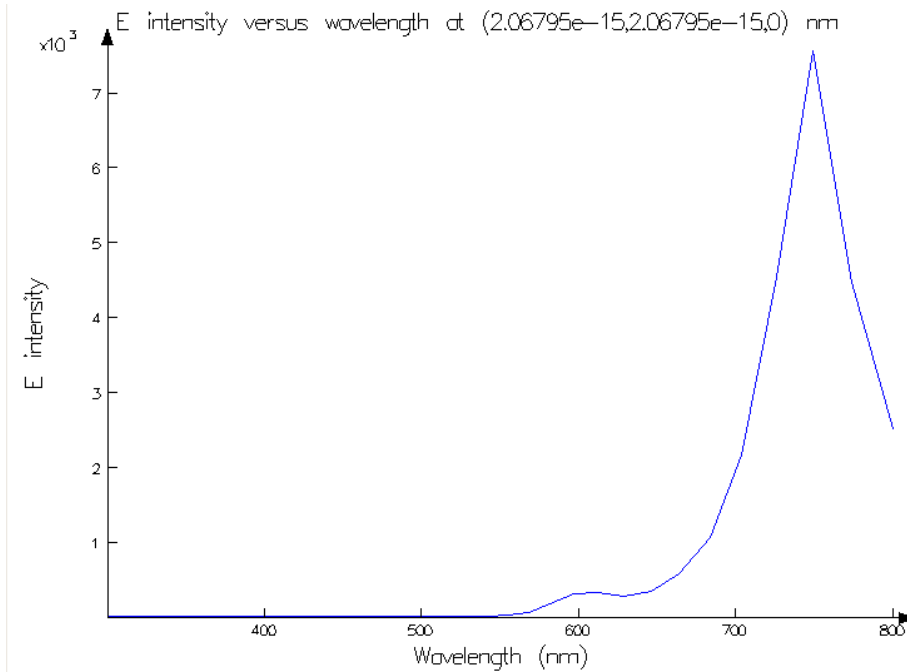


Figure 6.8: Electric field intensity of gold bowtie over wavelengths from 300 – 800nm at the origin. Thickness of structure in z direction is 30 nm, nanogap size is 10 nm.

Thirdly, for the 20nm thick bowtie with a 10nm gap, the most intense electric field was still in the inter-dimer region (Figure 6.11). At the origin the resonance wavelength was found to be 773.7nm, also about the same as the 40nm dimer and the other dimers with a gap spacing of 10nm. The local field intensity at this wavelength was 9.2×10^3 (Figure 6.10).

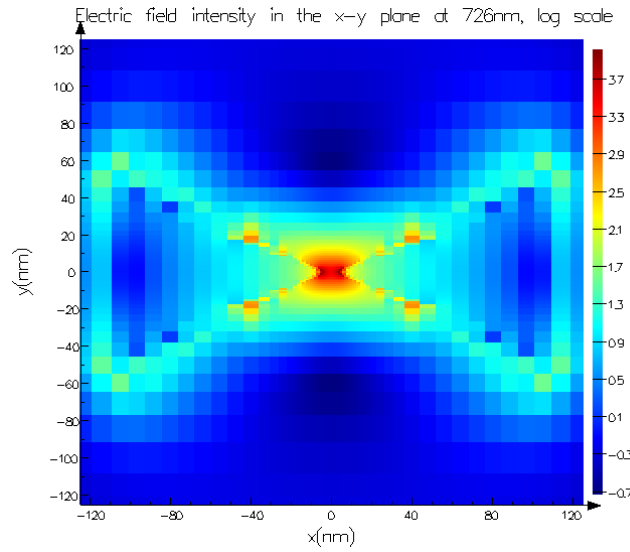


Figure 6.9: Electric field intensity of gold bowtie at resonance wavelength of 726 nm. Data taken in the x-y plane at $z = 0$ nm. Thickness of structure in z direction is 20 nm, nanogap size is 10 nm.

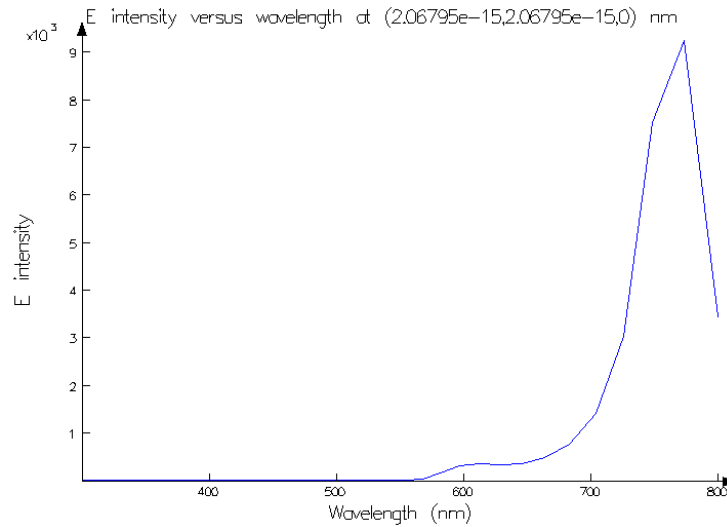


Figure 6.10: Electric field intensity of gold bowtie over wavelengths from 300 – 800nm at the origin. Thickness of structure in z direction is 20 nm, nanogap size is 10 nm.

Additionally, for the 40nm thick dimer with the larger nanogap of 20nm, the origin was again the location of highest field enhancement (Figure 6.11). Evaluated at the gap, the resonance wavelength was found to be about 725.9nm. The local field intensity at this wavelength was about 9.8×10^2 (Figure 6.12), smaller than any of the 10nm gap dimers.

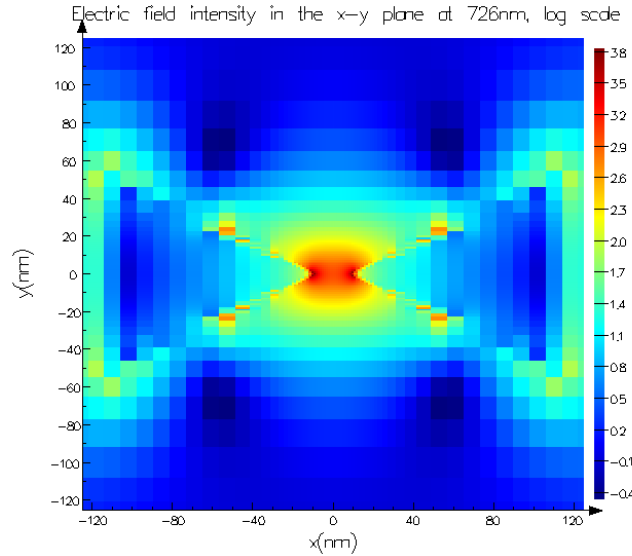


Figure 6.11: Electric field intensity of gold bowtie at resonance wavelength of 726 nm. Data taken in the x-y plane at $z = 0$ nm. Thickness of structure in z direction is 40 nm, nanogap size is 20 nm.

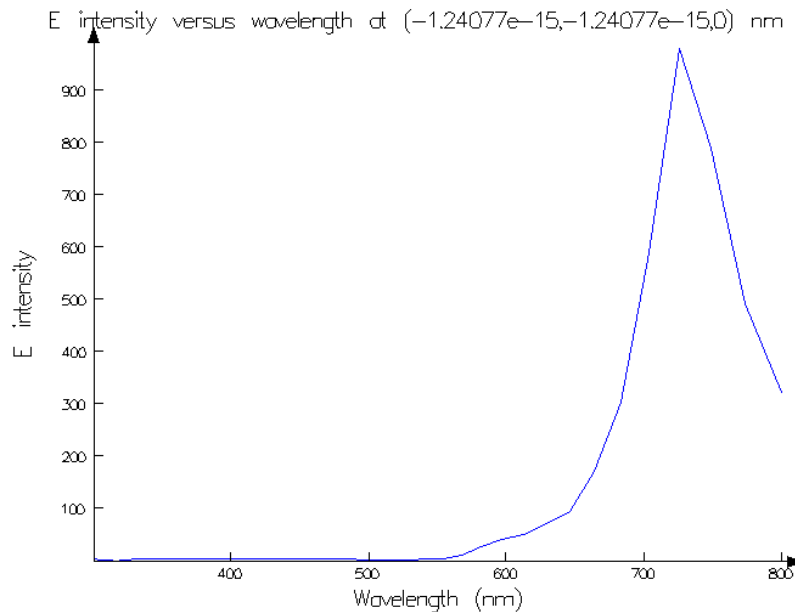


Figure 6.12: Electric field intensity of gold bowtie over wavelengths from 300 – 800nm at the origin. Thickness of structure in z direction is 40 nm, nanogap size is 20 nm.

6.3 Triangular Prism Dimer Array

For both the low-density and high-density gold triangular prism dimer arrays, the intensity versus position graphs for the initial tests with the 20-bowtie arrays implied that the nanogaps of the dimers closest to the origin were the locations of highest field enhancement (Figure 6.13, Figure 6.14).

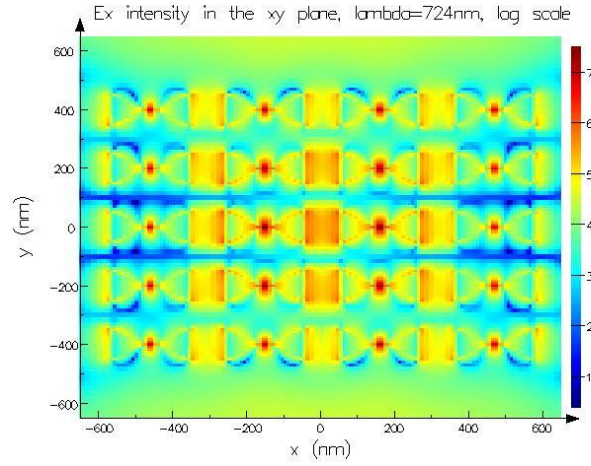


Figure 6.13: Initial test of electric field intensity of high-density gold bowtie array at resonance wavelength of 724 nm. Data taken in the x-y plane at $z = 0$ nm. Thickness of structure in z direction is 40 nm, nanogap size is 10 nm.

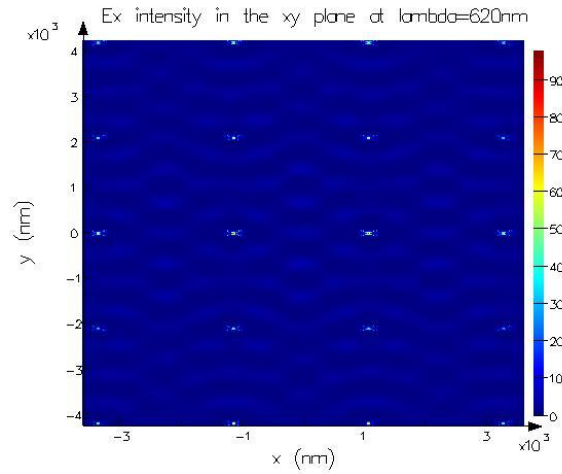


Figure 6.14: Initial test of electric field intensity of low-density gold bowtie array at resonance wavelength of 620 nm. Data taken in the x-y plane at $z = 0$ nm. Thickness of structure in z direction is 40 nm, nanogap size is 10 nm.

For the later simulation of the high-density array using periodic boundary conditions, the resonance wavelength at the center of the central dimer (Figure 6.15) appears to be 725.9nm. The local field intensity at this wavelength is approximately 3.8×10^3 (Figure 6.16). This is much lower than expected from the experimental results. For the low-density array with periodic boundary conditions, the results obtained changed with each plot. The electric field intensity appeared to be so small that it was difficult for the software to return a reading (Figure 6.17).

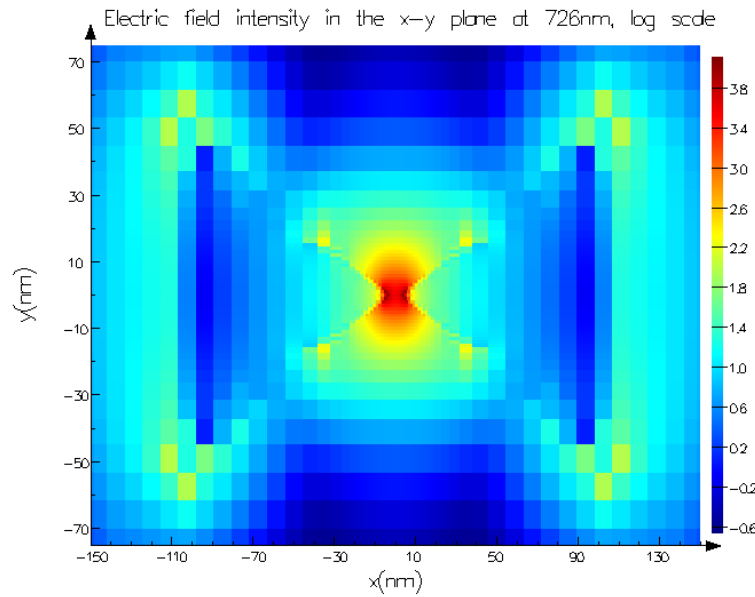


Figure 6.15: Electric field intensity of high-density gold bowtie array using periodic boundary conditions at resonance wavelength of 724 nm. Data taken in the x-y plane at $z = 0$ nm. Thickness of structure in z direction is 40 nm, nanogap size is 10 nm.

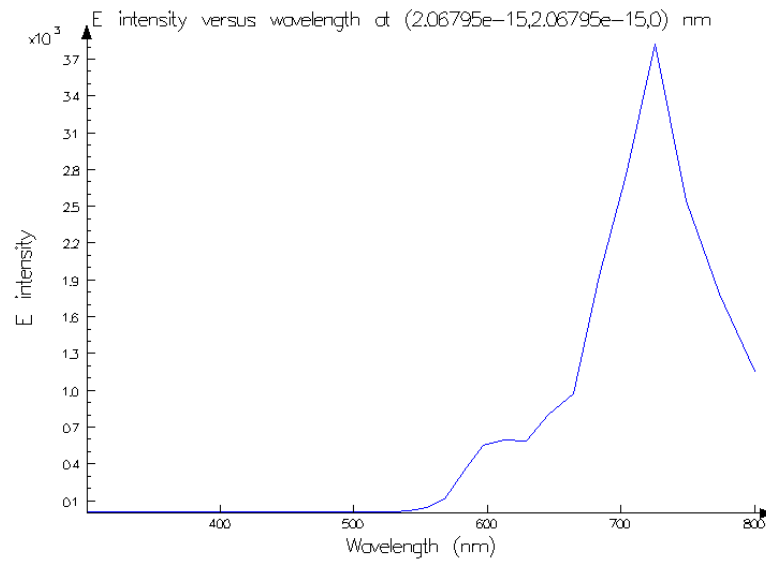


Figure 6.16: Electric field intensity of high-density gold bowtie array over wavelengths from 300 – 800nm at the origin.

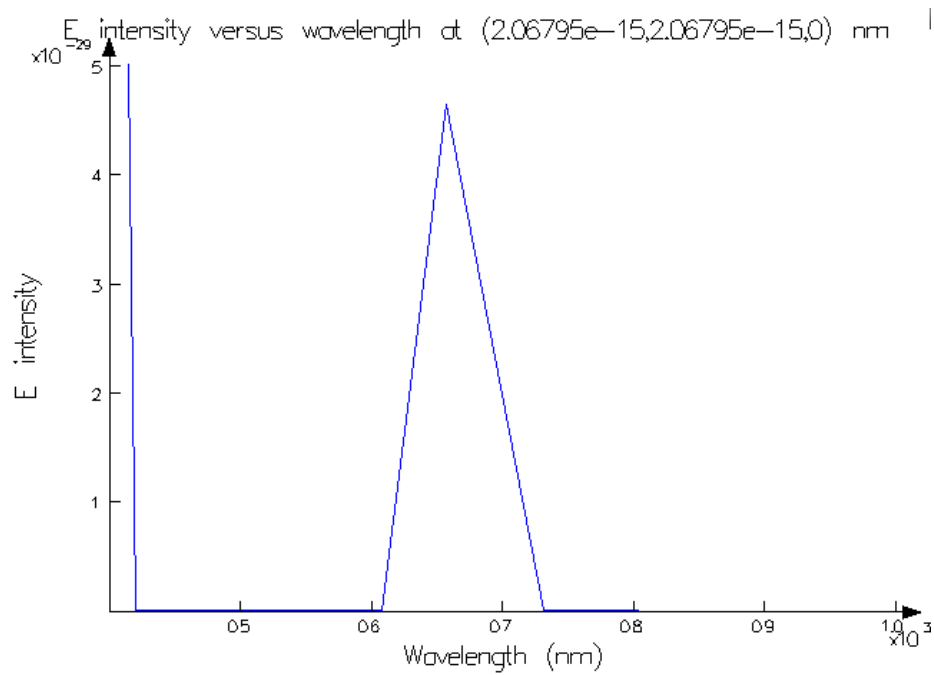


Figure 6.17: Inaccurate results of low-density gold bowtie array using periodic boundary conditions.

Chapter 7

Discussion

7.1 *Comparison with Computational Results*

For the nanospheres, highest resonance location was in the center of the nanogap, the same as in the calculated results. However, the resonance wavelength and the electromagnetic enhancement factors differed slightly. The $M^{EM} = |\mathbf{E}|^4 = 1.85 \times 10^7$ approximation is not far from the previously calculated value of approximately 6×10^6 [12]. Additionally, the FDTD simulation found the peak wavelength to be 440.4nm, rather than the 400nm in the Xu work. These results are similar but not identical.

Comparing the FDTD simulations in this work with the recent computational work done with bowtie arrays yields the observation that the resonant wavelengths were similar, even though the work by Dr. Hseuh's group contains much more detail from the experiment. However, the FDTD results of this work did not replicate the reported wavelength-position dependence inside the nanogap. The reported peak intensity for the bowtie array was approximately 1.8×10^3 , while the computational results from this work for the high-density array yielded a comparable value of 3.8×10^3 .

7.2 *Comparison with Experimental Results*

The trends for gap size and dimer thickness noted in the experimental results for the gold bowties arrays are mostly supported in these individual dimer simulations. The experimental and computational results in this work both imply that as the thickness of the nanoparticle increases past 40nm the scattered electric field intensity is degraded. However, the experimental results also noted

degradation in the enhancement for the 20nm thick bowtie. In the simulations, the smaller the thickness, the better the enhancement. This simulation does not account for the substrate or the molecular coatings on the dimers in the experiment. It is possible that these environmental factors are responsible. Another possibility is that internal losses from electron collisions are contributing to the lesser enhancement experimentally noted.

The experimental finding that as the nanogap size decreases, the electromagnetic field inside the gap dramatically increases is supported by the computational results. The change in the gap size is a much more dramatic effect than even the variations in thickness on the intensity of the electric field.

Comparison with the experimental trend of higher density array yielding higher enhancement values is inconclusive. The lack of data for the low-density array interferes with drawing any conclusions about the advantages of array density.

Chapter 8

Conclusion and Outlook

In this work, the optical properties of metal nanoparticle dimer and array geometries have been studied. The enhancement from the electromagnetic interaction of the metal nanoparticles with incident light has been computed using the finite-difference time-domain (FDTD) method. These results were compared with those from generalized Mie theory simulations and recent experimental work. Of particular interest are the predicted positions, wavelengths, and magnitudes of maximum electromagnetic enhancement for different nanoparticle geometries. These findings may serve as guidelines for future design of nanoplasmonic devices.

Future experiments seeking to greatly enhance the electric field in the interdimer region should include as small of a nanogap as is possible to manufacture in order to exploit the nanogap size trend noted both experimentally and computationally.

The results from the high-density array seem underreported compared to the experimental values for the enhancement factors. Further evaluation of this simulation, as well as new simulations at higher accuracies are needed to draw firm conclusions about the role of array density. From the enhancements noted on the dimers close to the origin, it seems that an array with a central dimer pair could allow even higher intensities in the nanogap of that central dimer.

Further studies should be done maintaining the volume of the nanoparticle while increasing the thickness to separate a size or volume effect from an effect directly related to the z-span height of the nanoparticle. Additionally, work to pinpoint the exact optimum thickness of the nanoparticle could be done.

It appears that the change in thickness did not change the location of the highest field enhancement: inside the nanogap. Likewise, the change in thickness of the dimers did not seem to shift the resonant wavelength drastically.

Since the effect of electromagnetic field enhancement is increased at sharp points in the nanostructures, studies of shapes with these characteristics should be done. Recent experimental work with gold nanostars [13] could be reproduced and refined with a computational simulation.

Precisely modeling experimental conditions for large arrays of dimers demands a large amount of memory. More accurate models including information about substrate structures and SERS molecules should be implemented on parallel computing systems to take advantage of the increased memory allowed by parallel computation and the ease of parallelizing the FDTD algorithm. The characteristics of the shapes experimentally generated could be more accurately reproduced with a more complex model by rounding hard points and including a model of the substrate, for instance.

Finally, the models described in this work are purely classical in their consideration of electromagnetic field behavior. For very small nanogap sizes between nanoparticle dimers, on the order of one angstrom, these models break down. In this regime, the wavefunctions of the electrons in the nanoparticles begin to overlap and hybridize; therefore, quantum mechanical models must be applied [32].

References

- [1] Montgomery, Jason M., Tae-Woo Lee and Stephen K. Gray. "Theory and Modeling of Light Interactions with Metallic Nanostructures." Journal of Physics: Condensed Matter (2008): 11pp.
- [2] Zhao, Linlin, et al. "Electrodynamics in Computational Chemistry." Northwestern University.
- [3] Engheta, Nader. "Circuits with Light at Nanoscales: Optical Nanocircuits Inspired by Metamaterials." Science (2007): 1698-1702.
- [4] Shuford, Kevin L., et al. "Optical Properties of Gold Pyramidal Shells ." Journal of Physical Chemistry C (2008): 6662-6666.
- [5] Raman, CV and Krishnan KS. "A New Type of Secondary Radiation". Nature. Vol 121. 501-502. 1928.
- [6] Jeanmaire, David L.; Richard P. van Duyne. "Surface Raman Electrochemistry Part I. Heterocyclic, Aromatic and Aliphatic Amines Adsorbed on the Anodized Silver Electrode". Journal of Electroanalytical Chemistry 84: 1–20. (1977).
- [7] Moskovits, Martin. "Surface-Enhanced Raman Spectroscopy: a Brief Perspective." Surface Enhanced Raman Scattering: Physics and Applications. Ed. Katrin Kneipp, Martin Moskovits and Harald Kneipp. Berlin: Springer, 2006.
- [8] Dieringer, Jon A., et al. "Surface enhanced Raman spectroscopy: new materials, concepts, characterization tools, and applications." Faraday Discussions 132 (2006): 9-26.
- [9] Willets, Katherine A. "Surface-enhanced Raman scattering (SERS) for probing internal cellular structure and dynamics ." Analytical and Bioanalytical Chemistry 394.1 (2009): 85-94.
- [10] Pieczonka, Nicholas P. W., Paul J. G. Goulet and Ricardo F. Aroca. "Applications of the Enhancement of Resonance Raman Scattering and Fluorescence by Strongly Coupled Metallic Nanostructures." Berlin, 2006.

- [11] Xu, Hongxing, et al. "Electromagnetic contributions to single-molecule sensitivity in surface-enhanced Raman scattering." Physical Review E 62.3 (2000): 4318-4324.
- [12] —. "Spectroscopy of Single Hemoglobin Molecules by Surface Enhanced Raman Scattering." Physical Review Letters 83.21 (1999): 4357-4360.
- [13] Hrelescu, Calin, et al. "Single gold nanostars enhance Raman scattering ." Applied Physics Letters (2009): 153113-1-153113-3.
- [14] Bakker, Reuben M., et al. "Near-field excitation of nanoantenna resonance." Optics Express 15.21 (2007): 13682-13688.
- [15] Foteinopoulou, S., J. P. Vigneron and C. Vandenbem. "Optical near-field excitations on plasmonic nanoparticle-based structures ." Optics Express 15.7 (2007): 4253-4267.
- [16] Schatz, George C., Matthew A. Young and Richard P. Van Duyne.
"Electromagnetic Mechanism of SERS." Surface Enhanced Raman Scattering: Physics and Applications. Ed. Katrin Kneipp, Martin Moskovits and Harald Kneipp. Berlin: Springer, 2006.
- [17] Fromm, David P., et al. "Gap-Dependent Optical Coupling of Single "Bowtie" Nanoantennas Resonant in the Visible." Nano Letters 4.5 (2004): 957-961.
- [18] Jain, P.K. and M.A. El-Sayed. "Noble Metal Nanoparticle Pairs: Effect of Medium for Enhanced Nanosensing." Nano Letters (2008): 4347-4352.
- [19] Zou, Shengli and George C. Schatz. "Coupled Plasmonic Plasmon/Photonic Resonance Effects in SERS ." Berlin (2006).
- [20] Zhao, Ke, et al. "One-dimensional arrays of nanoshell dimers for single molecule spectroscopy via surface-enhanced raman scattering." Journal of Chemical Physics 125.081102 (2006): 6.
- [21] Zoua, Shengli and George C. Schatz. "Silver nanoparticle array structures that produce giant enhancements in electromagnetic fields ." Chemical Physics Letters 403.1-3 (2005): 62-67.

- [22] Jiang, Jiang, et al. "Single Molecule Raman Spectroscopy at the Junctions of Large Ag Nanocrystals." Journal of Physical Chemistry B (2003): 9964-9972.
- [23] Lyandres, O., et al. Anal. Chem. 77.6134 (2005).
- [24] Taflove, Allen and Susan C. Hagness. Computational Electrodynamics: The Finite-Difference Time-Domain Method. 3rd Edition. Boston: Artech House, 2005.
- [25] Jackson, John David. Classical Electrodynamics. 3rd Edition. John Wiley and Sons, Inc., 1999.
- [26] Nahla A. Hatab, Baohua Gu and Gyula Eres. "Forthcoming." .
- [27] Hsueh, C. H., C. H. Lin and J. H. Li. "FDTD Simulations of Periodic Bowtie Nanostructures." Forthcoming .
- [28] Lumerical Solutions, Inc. Import Object Images. 14 May 2009
<http://www.lumerical.com/fdtd_online_help/user_guide_importing_images.php>.
- [29] —. Technology Trends: Overcoming the Multi-wavelength FDTD Challenge. 12 May 2009
<http://www.lumerical.com/fdtd_multicoefficient_material_modeling.php>.
- [30] Johnson, P. B. and R. W. Christy. Phys. Rev. B. Vol. 6. 1972.
- [31] Lumerical Solutions, Inc. FDTD Solutions Product Description. 14 May 2009
<http://www.lumerical.com/fdtd_parallel_description.php>.
- [32] Zhao, Ke et al. "Electronic Coupling and Optimal Gap Size between Two Metal Nanoparticles". Phys. Rev. Lett. 102, 186804 (2009).

Vita

Abigail Gaddis was born on October 1, 1984 in Shreveport, Louisiana. While progressing from kindergarten to high school, she attended school in public, private, and home settings. She graduated from Pickens High School in Pickens, South Carolina in June 2003. She next acquired a B.S. in Physics from Furman University, where she graduated cum laude in 2007. She then went to the University of Tennessee, Knoxville, receiving a M.S. in physics in 2009. She is currently pursuing her doctorate in Civil and Environmental Engineering at UT.